

Super-resolution for microwave breast cancer detection

Marco Miguel Valente Gomes
marco.v.gomes@tecnico.ulisboa.pt

Instituto Superior Técnico, Lisboa, Portugal
November 2023

Abstract— The development of super-resolution microwave imaging techniques has led to significant advancements in breast cancer diagnosis, a crucial field of medical diagnostics. This thesis explores the assessment and use of high-permittivity materials as lenses to improve the resolution of microwave imaging for the diagnosis of breast cancer, particularly agar and ultrasound gel. The research involves a comprehensive exploration of these high-permittivity materials. Through the assessment of their impact on image reconstruction and detection capabilities via numerical simulations and experimental testing, this study reveals promising outcomes in certain conditions. It highlights the efficacy of these materials in enhancing imaging resolution. Additionally, the study uncovers the limitations linked to high-permittivity materials in specific scenarios, providing insights into the intricate relationship between lens properties and their impacts on imaging capabilities. This highlights the intricate challenges and opportunities in optimizing breast cancer diagnostic technologies. Overall, this thesis explores the technologies and algorithms used in super-resolution microwave imaging for breast cancer detection. It provides insights into its potential, limitations, and the prospects for advancing diagnostic technologies.

Keywords— Anisotropic refractive index, Dielectric Slab, High-Permittivity materials; Microwave Imaging; Super-Resolution

I. INTRODUCTION

Nowadays, breast cancer is the most prevalent form of cancer worldwide [1]. One of the ways to increase the survival rate of the patients is by getting an early diagnosis of the disease, however the current diagnostic tools are limited. The techniques currently used for breast cancer detection, such as X-rays [2], [3], magnetic resonance imaging [4], and PET scans [5], possess numerous disadvantages including the use of ionizing radiation, high costs, and invasiveness. It is crucial to find a solution that minimizes these downsides while achieving the detection of similar tumors.

There are studies related to the use of microwave imaging to detect breast cancer [6]–[8]. This method uses radar techniques to detect the dielectric contrast between tumors and healthy breast tissue, yet the resolution of the images obtained by this method is not very high, because these systems are limited by Rayleigh's diffraction limit and can lead to false diagnosis.

II. STATE OF THE ART

A. Microwave imaging for breast cancer

Microwave imaging systems became to appear in the 1960s through the development of the radar and other similar sensors. These systems have multiple applications such as earth observation, weather forecasting, environmental monitoring, and medical imaging where microwaves are used to non-invasively detect and measure the properties of tissues of the human body.

The operating principle of these systems is based on the contrast between the permittivity of the different tissues in the breast. One or more antennas capture the electromagnetic energy that is scattered by these tissues.

Most of today's microwave imaging systems use frequencies in the band of 1GHz-10GHz (ISM band), there are certain constraints on the selection of frequencies, as a low frequency may result in a low resolution, while a high frequency may not be able to effectively penetrate the breast.[1]–[3]

There are multiple systems that use microwave imaging in controlled setups with a liquid that is used to do coupling with the measuring antennas[2], more recently there are studies revolving dry setups as these are more comfortable to the patient and there is no need to submerge the breast in a liquid[1].

There are two types of microwave imaging systems, monostatic systems where the same antenna is responsible for the transmission and reception of the signals and multistatic systems where a single antenna transmits a signal and multiple antennas receive it at different locations. Examples of these systems are represented in Figure II.1 for monostatic systems and Figure II.2 for multistatic systems.

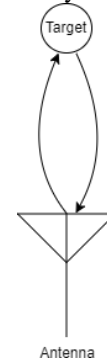


Figure II.1: Monostatic system

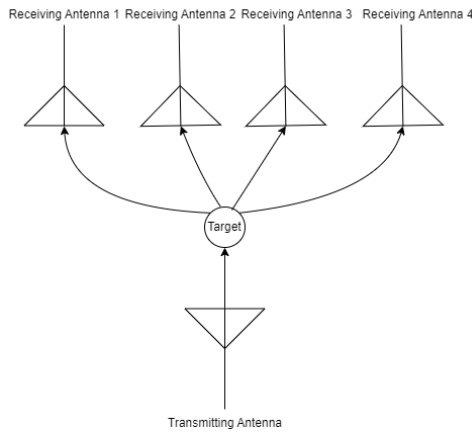


Figure II.2. Multistatic system

At the Instituto de Telecomunicações, work on microwave imaging for breast cancer with dry setups has been developed. To simulate breast tissues, a shell is filled with TX-100, a liquid with electromagnetic properties similar to those of the tissues found in the breast at the frequencies of interest. To simulate tumors, 3D printing using PLA filament has been utilized [1], [3].

Two antenna types were utilized: the XETS (cross exponentially tapered slot-based antenna) and the BAVA (balanced antipodal Vivaldi antenna). The XETS exhibits an extremely stable phase center across its entire frequency range of operation, while the BAVA is broadband and straightforward to manufacture [4]. The following figures show these antennas.

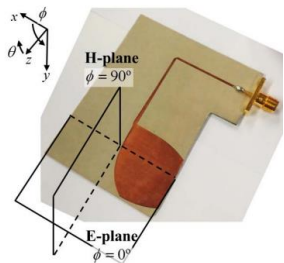


Figure II.3. BAVA Antenna (extracted from [4])

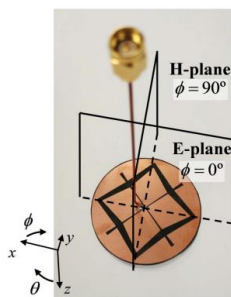


Figure II.4. XETS Antenna (extracted from [4])

Utilizing the XETS the obtained results were positive for tumors of large size but not that good for small tumors (inferior to 3 mm), as it can be seen by the figures below:

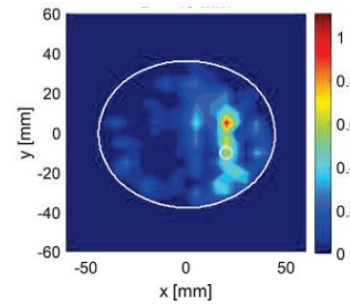


Figure II.5. Reconstructed image for 3 mm tumor (extracted from [3])

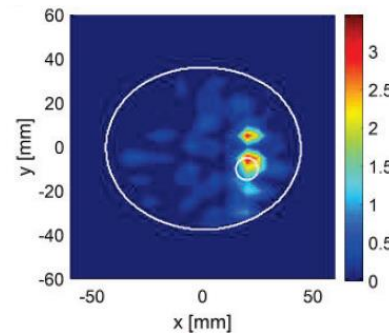


Figure II.6. Reconstructed image for 5 mm tumor (extracted from [3])

The poor results for small tumors are attributed to the limitation of current systems by Rayleigh diffraction. To address this issue, techniques such as super lenses are utilized to enhance the resolution of the acquired images.

B. Super-resolution Imaging

Super-resolution imaging is a set of techniques used to produce images with higher resolution than is possible with conventional imaging methods, breaking the Rayleigh's diffraction limit. This limit states that every imaging system that uses electromagnetic waves is limited to a resolution of $\lambda/2$, this happens because electromagnetic waves have a finite wavelength and when the size of the objects being imaged is smaller than half of the wavelength of operation it is not possible to represent them.

These techniques have been developed and refined over the past several decades and have found a wide range of applications in fields such as medicine, microscopy, and engineering[5]–[8].

Some authors ([7]–[11]) use machine learning approaches to increase the resolution of imaging systems, these approaches were proven to produce high resolution images, and are compatible with any conventional inverse scattering algorithm, but they have a major limitation which is the need to have a very extensive dataset to train the convolutional neural networks.

The physical approaches are more reliable because they don't need any previous knowledge of information about position of tumors or another data to train the neural networks.

Other authors [12]–[14] use complex materials with negative permittivity, obtaining decent super-resolution results. However, the materials used are quite complex to construct, and some of them are not suitable for the frequency band utilized in these kinds of applications [15].

One of these physical approaches ([16]) uses a metamaterial dielectric slab (which is a type of slab made from a material that has been artificially engineered to have specific electromagnetic properties that are not found in natural materials) with a high relative permittivity by stacking printed circuit boards with certain properties, and it was verified experimentally that the resolution increases with these types of super lenses.

To test the validity of the lens, two setups were carried out. The first setup consisted of a dipole horizontally traversing the lens with two targets behind it, and the second setup involved the same configuration but without the lens, to determine whether it was possible to detect the two targets. The results obtained are shown in Figure II.7

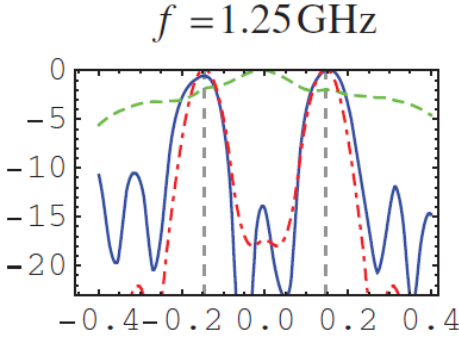


Figure II.7. Reflection coefficient in function of position (extracted from [16])

In Figure II.7 the magnitude of the reflection coefficient is shown as a function of the dipole position (normalized to the wavelength). The dotted grey line represents the true position of the two targets. The dotted green line indicates the result without the application of the lens, as can be seen it is not possible to detect the two targets without the lens. The blue line represents the result with the application of the lens, it is possible to see the well-defined detection of the two targets, with the S11 maxima in the target zone. The dotted red line represents the theoretical result calculated by the authors, which is very similar to the experimental result obtained in blue.

III. NUMERICAL AND SIMULATION RESULTS

A. Super Resolution validation and imaging

To validate the state-of-the-art results on super-resolution [17], a comparable scenario was tested. Using CST [18], a simulation was conducted for a similar setup as depicted in Figure III.1.

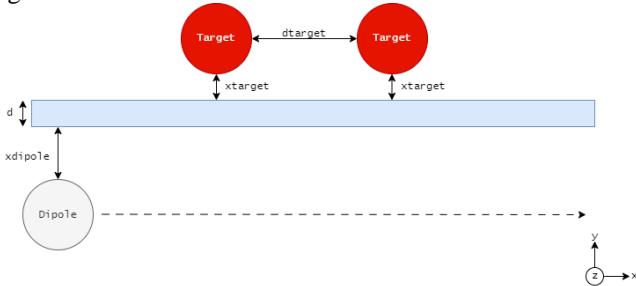


Figure III.1. Geometry of the simulations for super resolution validation

In Figure III.1 it is represented the generic geometry of multiple setups, with a lens of thickness d two targets with a distance d_{target} between them and x_{target} between each one to the lens, a dipole with a distance x_{dipole} from the antenna to the lens.

With this geometry four setups were made:

- Dipole in free space with no targets
- Dipole in free space with two targets
- Dipole with a lens and no targets
- Dipole with a lens and two targets

To verify the efficacy of the proposed microwave imaging system, various experimental configurations were designed and implemented. A lens of thickness $d = 1 \text{ mm}$, determined using Equation 2.4, was utilized in these simulations. A scan was done on the x -axis, varying the position of the antenna by 5 mm in 5 mm in a region of -100 mm to +100 mm. These configurations were chosen to study the performance of the imaging system under a range of different conditions and to validate the theoretical concepts.

Using MATLAB[19], the S parameters were extracted from the CST [18] simulation, encompassing the responses of both the targets, the lens and the antenna. In order to obtain the reflection coefficient of the targets only, it was necessary to calibrate the S11 parameter, knowing that the S11 obtained from the simulations of the dipole in free space with two targets contains the reflection coefficient of the antenna and the target and that the S11 obtained from the simulations of the dipole in free space with no target contains the reflection coefficient of the antenna, it becomes trivial to obtain only the S11 of the target, by subtracting the S11 of one simulation from the other.

The following graph was then obtained, presenting the calibrated S11 as a function of position (in x), for a frequency of 5.5 GHz which is the resonant frequency of the utilized dipole.

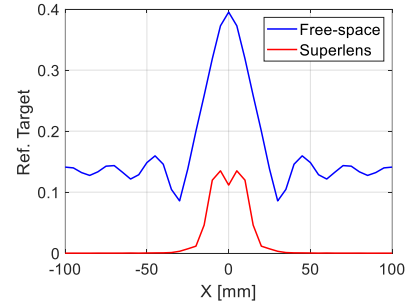


Figure III.2. Super Resolution with water lens and dipole

For the generation of this graph, the utilized setup is illustrated in Figure III.1 with $d = 1 \text{ mm}$ (to propagate only one mode within the dielectric slab), a lens permittivity of 78 (employing a water lens with losses), $x_{dipole} = 3.5 \text{ mm}$, $x_{target} = 3.5 \text{ mm}$, and $d_{target} = 8.63 \text{ mm}$ (equivalent to approximately $\lambda/6$ in free space). As depicted Figure III.2, in the case of testing detection in free space, it is evident that no distinction can be made between the two targets. This is attributed to the electromagnetic wave being constrained by

Rayleigh diffraction. However, when the water lens is introduced (serving as a dielectric slab due to its significantly high permittivity), despite obtaining a response with lower amplitude (attributed to the substantial losses in water), a distinction between the targets at the correct positions (with $d_{target} = 8.63\text{mm}$) becomes perceptible. Consequently, the results observed in the state-of-the-art are validated.

To utilize the image reconstruction algorithm, it is necessary to calculate the refractive indices, according to x and according to z . In this case, the refractive index according to z will be the refractive index of the medium itself. For the analysis of distance in free space, $n = 1$, and for the analysis of distance within the lens, $n = \sqrt{78}$ (refractive index of water) is considered. To calculate the refractive index according to x , the following setup was simulated, as depicted in Figure III.3 in two situations. The first involves placing an embedded active dipole within the water lens, and another passive dipole serving as a target at 10 mm. The second situation excludes the consideration of the passive dipole, leaving only the lens and the active dipole. In these simulations, the S11 parameters were exported to calculate the target response as a function of distance (by subtracting the S11 from the simulation with both dipoles from the S11 of the simulation with only the active dipole). This approach allows for the calculation of the electrical distance between dipoles, visualizing the distance corresponding to the maximum intensity of the target response.

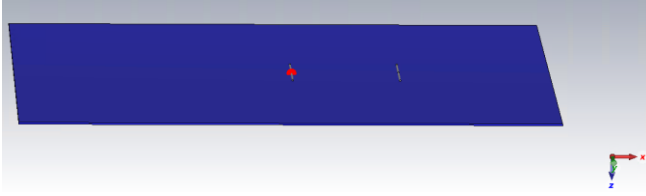


Figure III.3. Setup for the n_x calculation

With this setup, it was obtained the following graph with the target response which is the difference between s11 with active dipole, lens and passive dipole and s11 with active dipole and lens in function of the distance:

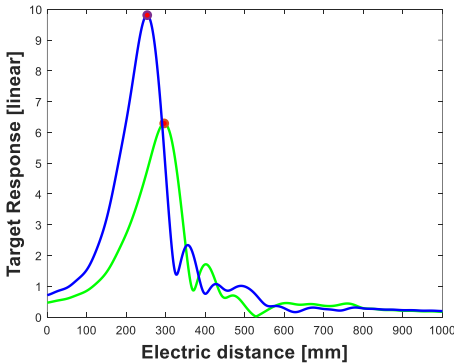


Figure III.4. Target response in function of the electric distance

In Figure III.4, the blue curve represents the response of the target with the passive dipole placed 50 mm from the active dipole, while the green curve represents the response with the passive dipole placed 60 mm from the active dipole. The electrical distances obtained are 253 mm for the blue curve and 296 mm for the green curve. In both situations, the active

dipole is positioned at the center of the plate. The refractive index according to x is calculated using the following expression:

$$n_x = \frac{d_{e1} - d_{e0}}{d_1 - d_0} \quad (III.1)$$

Where d_{e1} and d_{e0} are the electrical distances of the further and closest position of the target respectively and d_1 and d_0 are the physical distances of the further and closest position of the target respectively. With this expression, the refractive index in the x direction is approximately 4.3.

With the refractive index calculated in both directions, it is now possible to employ the image reconstruction algorithm, resulting in the following images:

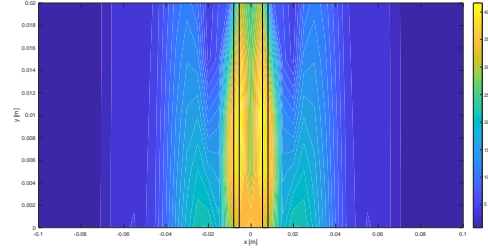


Figure III.5. Obtained image with the algorithm, with lens

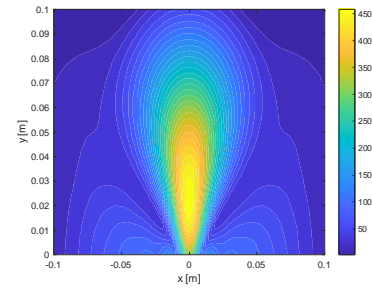


Figure III.6. Obtained image with the algorithm, in free space

In the image, a distinction among the targets is evident when the lens is present, revealing a separation between the targets (d_{target}) of 8.63mm. This differentiation is not observed when the targets are in free space, where there is no distinction between the targets, resulting in a merging of the responses of both targets at the center of the image.

B. Lens Attenuation

To verify the calculations of attenuation in an asymmetric dielectric slab (as is the case in the final setup, where medium 0 is air, medium 1 is the lens with a permittivity approximately equal to 78, and medium 2 is the breast with a permittivity approximately equal to 4), a simulation was performed. A setup was created with a dipole placed 2mm from the lens, operating at 6 GHz, a water lens (permittivity equal to 78), and a parallelepiped representing the breast material (permittivity = 4) immediately following the lens, as depicted in the figures below

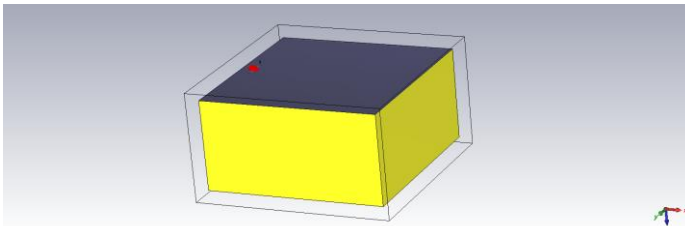


Figure III.7. Setup of the attenuation simulation (perspective view)

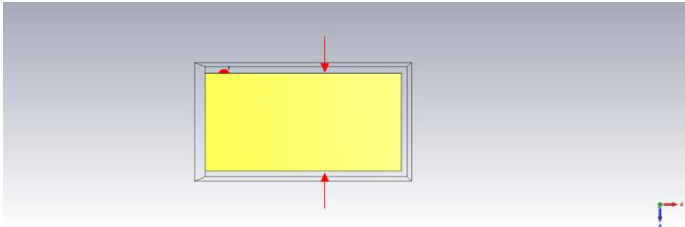


Figure III.8. Setup of the attenuation simulation (front view)

In this setup, the near-field electric field was simulated as a function of distance in the z -direction, assuming a constant x of 20mm from the center of the lens (marked by the red arrows, in the front view). it was defined an attenuation as:

$$Att = |20 \log(E[p1]) - 20 \log(E[p2])| \quad (4.2)$$

Where $E[p1]$ and $E[p2]$ are the values of the RMS near field for $z = 1\text{mm}$ and $z=2\text{mm}$ respectively.

With this equation it is possible to plot the Attenuation in function of frequency obtaining the following graphs for different values of slab thicknesses and permittivity.

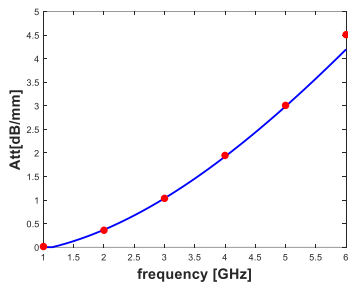


Figure III.9. Attenuation for a lens with thickness = 1 mm and permittivity = 78

It is concluded that empirical results validate theoretical equations, indicating an increase in attenuation with frequency in this case, as well as an increase in attenuation with the permittivity of the slab.

The bandwidth for each scenario is measured in gigahertz (GHz), and as observed in the table, dielectric slabs with smaller thicknesses can provide twice the bandwidth where only one mode propagates. This bandwidth will increase with a decrease in the permittivity of the slab.

To achieve super-resolution, there needs to be a surface wave exciting the dielectric plate and adhered to it to create evanescent fields. In this setup, a dipole designed at 5.5 GHz was placed entirely embedded in the lens, 15 mm from the beginning of the lens (in the x -direction) with a thickness of 1 mm and permittivity of 78. A parallelepiped with breast

properties and a thickness of 100mm (permittivity equal to 4) was then simulated for the electric field at $y=0$ in two situations: the first for a frequency of 500 MHz, where no mode is expected to propagate, and the second for a frequency of 5 GHz, where a mode propagates within the slab. The results are presented in the figures below.

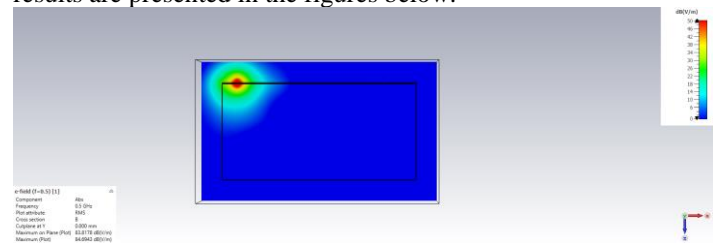


Figure III.10. Propagation inside the slab at 500 MHz

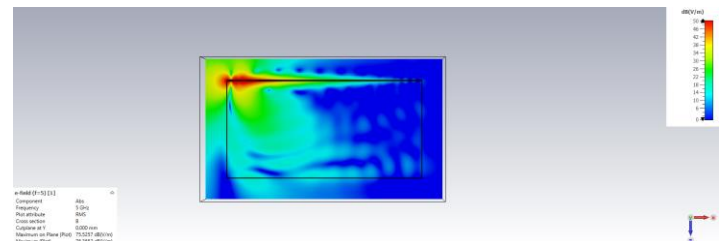


Figure III.11. Propagation inside the slab at 5 GHz

As seen in the figures above, for a frequency outside the propagation bandwidth of the slab (500MHz), no mode propagates within the slab, indicated by a null electric field. However, for 5 GHz, propagation within the slab is evident from the electric field, which is highly confined within.

C. Super Resolution Detection Simulation

Prior to conducting any experimental tests, simulations were necessary to determine if it was possible to detect small superficial tumors. To achieve this, CST was used, utilizing a dielectric slab of water (permittivity 78) with a thickness of 1 mm, placed above a 20 mm slab with a permittivity of 4, representing the breast. A dipole designed for 5.5 GHz was positioned 2mm away from the lens (in the z -direction), and two PEC (Perfect Electric Conductor) cylinders were embedded in the breast with a spacing of 14 mm between them at depths ranging from 0 to 4 mm, to test the detection capability, this setup is represented in Figure III.12.

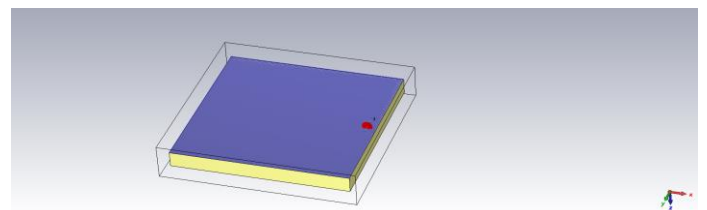


Figure III.12. Detection Simulation Setup

Using the image reconstruction algorithm, images were generated for depths ranging from 0 to 4 mm and for two slabs with a permittivity of 78, varying the thickness from 1 mm to 0.5 mm. The results for the first slab (thickness = 1 mm) at

depths of 0, 1, 2, and 3 mm are presented in Figure III.13 and Figure III.14..

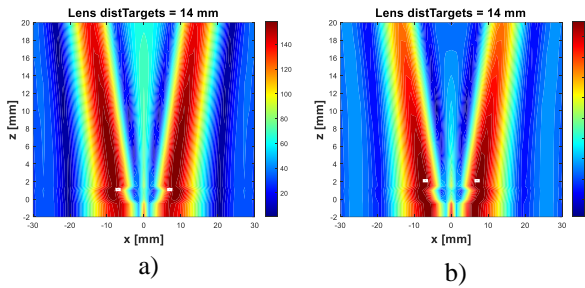


Figure III.13. 2D Image for depth = 0 mm (a) and 1 mm (b)

In these first two images, where the depth is 0 and 1 mm, it is possible to observe the detection of two targets in the correct positions, with a distance between targets of 14 mm (less than $\frac{\lambda}{2}$ in the breast, surpassing the Rayleigh diffraction limit). There is also a decrease of 50 in linear units, equivalent to an attenuation of approximately 2 dB/mm, which is roughly in line with the theoretical calculations.

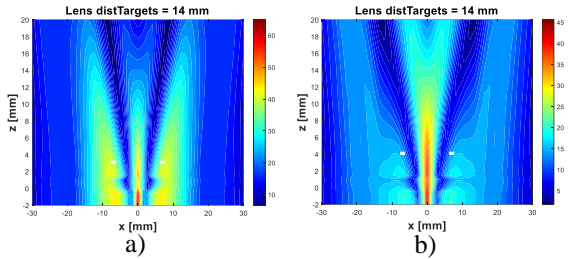


Figure III.14. 2D Image for depth = 2mm (a) and 3mm (b)

Based on the results obtained from a depth of 3 mm, it is no longer possible to detect tumors separated by 14 mm, as the responses of both tumors are summed in the center of the image. This further confirms the attenuation of 2 dB/mm obtained in the previous figures, affirming the detection capability primarily for superficial tumors.

Since in a real situation, the breast is more similar to a cylinder than a parallelepiped, the following structure, as represented in the figure below, was simulated. In this structure, the breast is represented by a cylinder with a radius of 50 mm and a height of 100 mm. A dielectric slab in the shape of an arc is placed around the breast, and a dipole designed for 5.5 GHz is positioned 2 mm away from the lens. The dipole performs a circular sweep around the breast, scanning the breast over 180 degrees and taking measurements every 6 degrees. Two PEC targets are embedded, spaced 10 mm apart, and placed at a depth of 0 mm in the first simulation and 1 mm in the second simulation. The same scenarios were also simulated without the lens for comparison. The setup for a depth of 0 mm, with a 1 mm-thick lens and permittivity of 78, is depicted in the figure below.

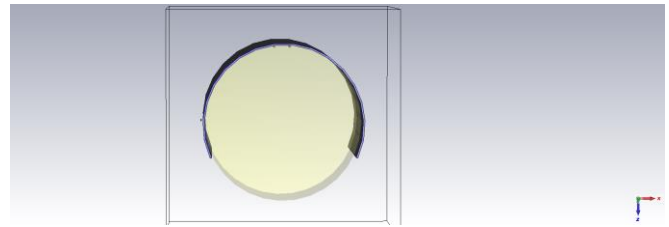


Figure III.15. Setup for cylindrical breast

The image reconstruction algorithm was used to generate a 2D image. These results are presented in the figures below:

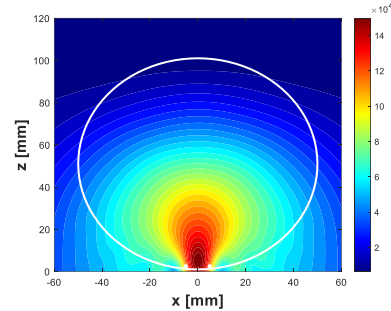


Figure III.16. 2D Image for detection with no lens

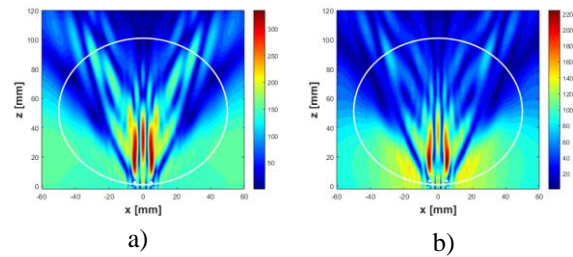


Figure III.17. 2D Image for detection with lens for a depth of 0 mm (a) and 1 mm (b)

From the images above, it is possible to observe that without the lens, there is no detection, with the response of the two targets interacting in the center of the image. With the lens, detection is achieved between targets spaced 10 mm apart. When the targets are placed at a depth of 1 mm, a decrease in amplitude from 300 to 220 is observed, which translates to an attenuation of approximately 1.4 dB/mm. This result is very similar to what was theoretically expected for this frequency band.

IV. EXPERIMENTAL RESULTS

A. Detection with symmetrical slab

Several experimental tests were conducted to validate the numerical and simulated results. Prior to any experimental testing, various materials were examined for their suitability in creating a high-permittivity solid lens. Three materials were proposed, including agar (a polysaccharide commonly used in culinary applications to make gelatin) ultrasound gel, and aloe vera gel. The permittivity and conductivities of these three materials were tested to determine if they possessed the desired properties for constructing the lens, using the Coaxial probe method [20]. The results of the permittivity and

conductivities are presented in the figures below for all three materials.

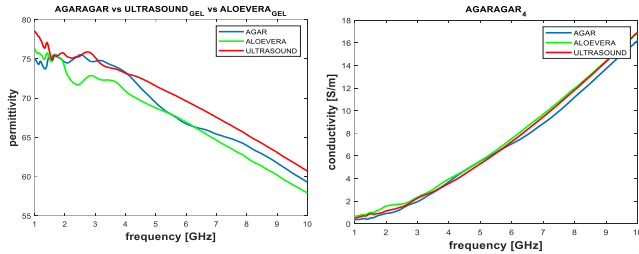


Figure IV.1. Permittivity and conductivity vs frequency

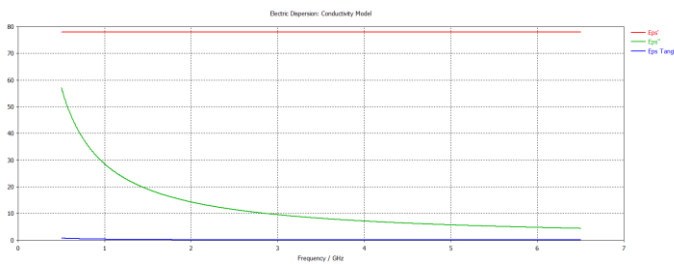


Figure IV.2. Permittivity and $\tan\delta$ of water

These results were generated to enable comparison with the permittivity of water (presented in Figure IV.2), to determine if they were good candidates for use as lenses to achieve super-resolution. It is the high permittivity that allows for the creation of evanescent fields not physically constrained by Rayleigh diffraction.

Based on these results, it is possible to conclude that all these materials could be potential solutions for creating the lens, as their permittivity is very close to that of water, effectively functioning as dielectric slabs.

These three materials were subsequently tested for manufacturing a dielectric slab. However, it was observed that aloe vera gel was a low-viscosity material, resulting in a very liquid lens that made measurements difficult. Therefore, the decision was made to exclude this material, and lenses were fabricated using the remaining materials.

To create the agar lens, a frame measuring 180x180x1 mm was 3D printed, using PLA, to hold the lens structure. This frame was attached to an acetate sheet. Then, a homogeneous solution was prepared with 6g of agar powder and 250ml of water. The solution was heated until it began to boil and was poured into the frame. Finally, another acetate sheet was placed over the frame, covering the homogeneous solution, and the mixture was evenly spread.

For the ultrasound gel lens, ultrasound gel was applied over an identical frame with the acetate sheet attached underneath. Another acetate sheet was placed on top to spread the gel uniformly.

The first experimental test served as a proof of concept, aiming to verify the detection in symmetric dielectric slabs and compare these results with those obtained through simulation. The setup used closely resembled the one utilized in the simulations, involving a dipole located approximately 2 mm from the lens, designed for 6 GHz, with the same orientation of the targets. The targets employed consisted of two aluminum pieces, each with a thickness of approximately 0.1 mm and a width of 1 mm, mirroring the simulation

conditions. These targets were tested for various values of distTargets (target separation). The setup is depicted in Figure IV.3 and Figure IV.4 for the configurations without a lens and with a lens, respectively.

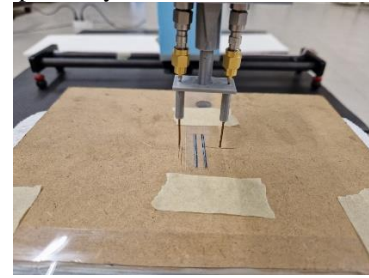


Figure IV.3. Experimental setup (without lens) for symmetrical slab

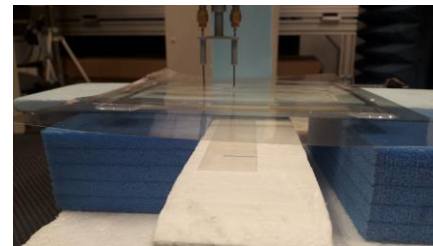


Figure IV.4. Experimental setup (with lens) for symmetrical slab

With the setups depicted in the figures above, measurements of the S11 were conducted, mirroring the simulation approach, but this time utilizing a Vector Network Analyzer (VNA). For distances between targets of 14 and 5.5 mm were tested with lens, and 14 mm without lens. The results are presented in the figures below.

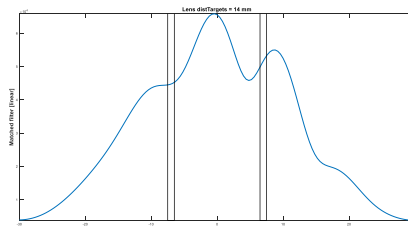


Figure IV.5. Image without lens with $\text{distTargets} = 14 \text{ mm}$

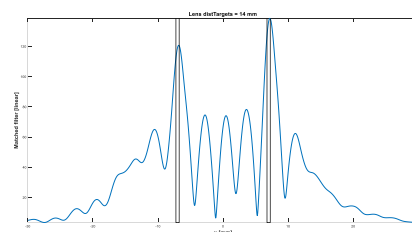


Figure IV.6. 1D Image for Agar Lens with $\text{distTargets} = 14 \text{ mm}$

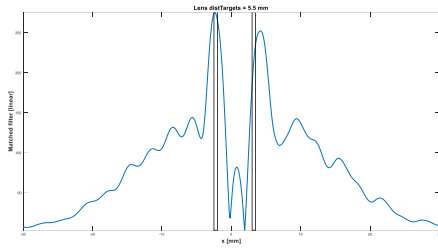


Figure IV.7. 1D Image for Agar Lens with $distTargets = 5.5$ mm

In all these images, the frequency band used ranged from 5 to 6 GHz (where only one mode propagates within the slab). Based on the results obtained, it is possible to observe detection in the cases with the lens, for the different separation distances. This is not observed in the case where the setup does not have a lens, as it is limited by Rayleigh diffraction. The maximum resolution that could be achieved without a lens in this case would be 50 mm ($\frac{\lambda}{2}$). As a result, no resolution is obtained for separation distances between targets that are less than this value, as seen in Figure IV.5

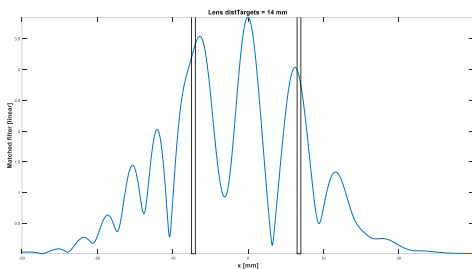


Figure IV.8. 1D Image for Ultrasound Gel Lens with $distTargets = 14$ mm

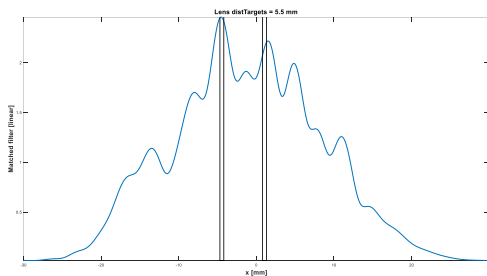


Figure IV.9. 1D Image for Ultrasound Gel Lens with $distTargets = 5.5$ mm

For the ultrasound gel lens, the conclusions are similar (targets can be detected up to a 5.5 mm separation). However, there is a much greater interaction between the targets compared to the agar lens. This may be attributed to various factors, such as the ultrasound gel lens being a less homogeneous structure compared to the agar lens. Ultrasound gel is more viscous and less easily spread than agar, when agar is in a liquid state which complicates the process of fabrication of this lens.

B. Detection with asymmetrical slab

To experimentally test an asymmetric dielectric slab setup, a CD case was filled with Triton X-100, a laboratory detergent that simulates the electromagnetic properties of breast tissue (with a permittivity approximately equal to 4)[21]. An agar lens, fabricated in the same manner as the symmetric setup, but with a frame, 3D printed with TPU, so it can be bended and attached to the CD case using adhesive tape, as observed in Figure IV.11. The used antenna was a dipole designed for 4.9 GHz. The dipole swept through an angle range of 315° to 45° around the CD case. Tumors were represented by cylindrical metal rods with a 6 mm diameter, placed at center-to-center separations of 30 mm, 20 mm, and 10 mm and at depths of 0 mm, 7 mm, and 14 mm within the case representing the breast.

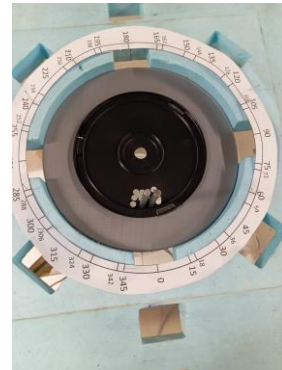


Figure IV.10. Setup for Radial measurements

As observed in the image above, the targets are centered at 0° . The CD case was perforated to allow the placement of the metal rods at different positions and depths, with the aim of testing detection in various scenarios, mirroring the simulations conducted and presented in III. The figure below depicts the front view of the setups used for measurements with target separation of 30 mm, corresponding to a setup with an agar lens.



Figure IV.11. Front view for radial setup with lens and $distTargets = 30$ mm

As seen in the figure above, the targets were positioned to be upright and parallel. This was done to ensure that, during the antenna's sweeping motion, there would be no interference from the targets in a lower plane. The goal was to minimize reflections from other planes by conducting the sweep solely in one plane.

For comparison, images were generated without the lens, presenting them in the figures below:

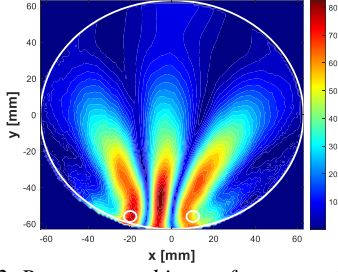


Figure IV.12. Reconstructed image for setup with no lens, with $distTarget = 24$ mm

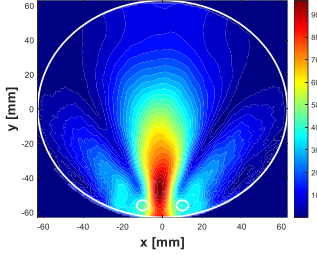


Figure IV.13. Reconstructed image for setup with no lens, with $distTarget = 14$ mm

From the images obtained without a lens above, it can be concluded that there is detection in the first scenario, as expected, given that the distance between the targets is greater than $\lambda/2$. However, as the targets move closer together, with 14 mm between them (which is less than $\lambda/2$ within the breast), there is only a combined response of the two targets, leading to no detection.

With lens, the results were the following:

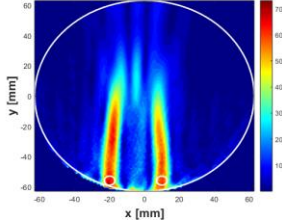


Figure IV.14. Reconstructed image for setup with lens, with $distTargets = 24$ mm, $depth = 0$ mm

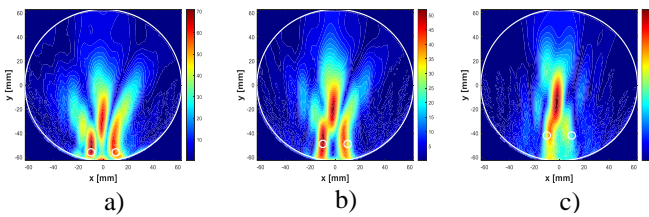


Figure IV.15. Reconstructed image for setup with lens, with $distTargets = 14$ mm, a) $depth = 0$ mm b) $depth = 7$ mm c) $depth = 14$ mm

In this case, where the targets are closer, maintaining a distance between centers of 20 mm (equivalent to $distTargets = 14$ mm), detection is observed when the targets are at a depth of 0 mm and at a depth of 7 mm. This did not occur in the results without the lens (due to the system being limited by Rayleigh's diffraction). These figures show clear evidence of

super-resolution with the use of the agar lens within a medium with electromagnetic properties similar to those of the breast. In c), it is evident that the attenuation is already too high, making it impossible to distinguish the targets, resulting in a combined response rather than separate responses from both targets.

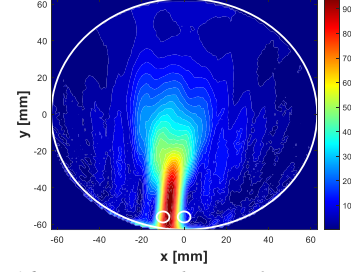


Figure IV.16. Reconstructed image for setup with lens, with $distTarget = 14$ mm, $depth = 0$ mm

In this last case, it was not possible to achieve detection, resulting in a clear image showing the sum of the responses from the two targets in the center. This outcome indicates that for a target separation distance of 4 mm, it is not feasible to achieve detection using the agar lens employed. No other depths were tested, as detection was not obtained at a depth of 0 mm.

V. CONCLUSION

This research explores the use of high-permittivity materials to enhance microwave imaging for breast cancer detection. Its significance lies in revealing the potential of these materials, such as agar and ultrasound gel, to amplify imaging resolution, offering promise for more effective diagnostic techniques in breast cancer detection.

Through this research, the fundamental mechanism of electromagnetic wave propagation in dielectric slabs has been studied, both in symmetric cases (where targets are in free space) and asymmetric cases (where targets are embedded in a medium with a different permittivity than air). Numerical methods and simulations were employed to verify this study, aiming to obtain confirmatory results. The primary challenges in this research lie in finding a balance between frequency and the dielectric slab's thickness (lens) to minimize attenuation and maximize detection. However, achieving this balance is complex because, while increased frequency enhances detection, it also drastically raises attenuation within the breast, resulting in insufficient signal for target detection (tumors).

The main objective of the work was to achieve superior resolution within the breast compared to the resolution obtained by the existing state-of-the-art microwave imaging mechanisms, which do not utilize these super-resolution techniques for better detection. This objective was met, both through simulations and experimental validation. In simulations, an approximate resolution of $\lambda/3$ was obtained for the maximum frequency used, with PE of approximately 3 mm, potentially due to the consideration of a Cartesian geometry in the image reconstruction algorithm and an approximation of the refractive index through frequency using the developed n_x selection algorithm. Experimentally, the

achieved resolution was greater than $\lambda/2$ for the maximum frequency used, with PE of approximately 0, as the targets' detection was practically in their actual positions. These results demonstrate that a super lens can enhance breast cancer detection in a way that would not be feasible with a conventional setup without utilizing materials of very high permittivity.

The novelty of the thesis lies in the enhancement of breast cancer detection through the application of super-lenses in microwave imaging. Unlike existing state-of-the-art mechanisms, the study utilizes high-permittivity existing materials, such as agar and ultrasound gel, as lenses to improve resolution and detection capabilities. This innovative approach enables the attainment of superior resolution within the breast area compared to conventional microwave imaging, offering better detection and potentially overcoming the limitations of current imaging technologies.

VI. ACKNOWLEDGMENT

I would like to thank Professor Carlos Fernandes for the challenge proposed in this thesis, for all the feedback provided during its development, with comments and suggestions that piqued my interest and encouraged me to explore further. To Professor João Felício, thank you for all the time and patience you dedicated to helping me understand complex concepts and for the continuous support in the laboratory. Thanks to Raquel Martins for the availability to assist in in the setups and for the creative ideas provided to facilitate the work. A big thank you to Professor David Fernandes and Professor Sérgio Matos for all the suggestions and constructive criticism provided during meetings, which helped me gain a better understanding of the concepts and made the work more comprehensible.

I would also like to thank Instituto de Telecomunicações for providing all the infrastructure necessary to carry out the thesis, this work was funded by Fundação para a Ciência e Tecnologia (FCT/MCTES) and co-funded by FEDER-PT2020 partnership agreement under projects UIDB/50008/2020 and 2022.04764.PTDC (IRMIS).

Finally, I would like to express my gratitude to my family and friends, whose unwavering support and encouragement helped me complete this work.

REFERENCES

- [1] J. M. Felício, J. M. Bioucas-Dias, J. R. Costa, and C. A. Fernandes, "Microwave Breast Imaging Using a Dry Setup," *IEEE Trans Comput Imaging*, vol. 6, pp. 167–180, 2020, doi: 10.1109/TCLI.2019.2931079.
- [2] N. K. Nikolova, "Microwave imaging for breast cancer," *IEEE Microw Mag*, vol. 12, no. 7, pp. 78–94, Dec. 2011, doi: 10.1109/MMM.2011.942702.
- [3] R. A. Martins, J. M. Felício, J. R. Costa, and C. A. Fernandes, "Systematic Analysis of Microwave Breast Imaging Detection of Different-Sized Malignant and Benign Tumors; Systematic Analysis of Microwave Breast Imaging Detection of Different-Sized Malignant and Benign Tumors," 2022.
- [4] J. M. Felício, J. M. Bioucas-Dias, J. R. Costa, and C. A. Fernandes, "Antenna Design and Near-Field Characterization for Medical Microwave Imaging Applications," *IEEE Trans Antennas Propag*, vol. 67, no. 7, pp. 4811–4824, Jul. 2019, doi: 10.1109/TAP.2019.2905742.
- [5] M. Tabib-Azar, J. L. Katz, and LeClair, "Evanescent microwaves: a novel super-resolution noncontact nondestructive imaging technique for biological applications," *IEEE Trans Instrum Meas*, vol. 48, no. 6, pp. 1111–1116, 1999, doi: 10.1109/19.816123.
- [6] M. G. Silveirinha, C. R. Medeiros, C. A. Fernandes, and J. R. Costa, "Experimental verification of broadband superlensing using a metamaterial with an extreme index of refraction," *Phys Rev B Condens Matter Mater Phys*, vol. 81, no. 3, Jan. 2010, doi: 10.1103/PhysRevB.81.033101.
- [7] Y. Kondo, X.-H. Han, and Y.-W. Chen, "Two-step learning based super resolution and its application to 3D medical volumes," in *2015 IEEE 4th Global Conference on Consumer Electronics (GCCE)*, IEEE, Oct. 2015, pp. 326–327. doi: 10.1109/GCCE.2015.7398738.
- [8] L.-Y. Xiao, R. Hong, L.-Y. Zhao, H.-J. Hu, and Q. H. Liu, "A Hybrid Neural Network Electromagnetic Inversion Scheme (HNNEMIS) for Super-Resolution 3-D Microwave Human Brain Imaging," *IEEE Trans Antennas Propag*, vol. 70, no. 8, pp. 6277–6286, Aug. 2022, doi: 10.1109/TAP.2022.3146571.
- [9] P. Shah and M. Moghaddam, "Super resolution for microwave imaging: A deep learning approach," in *2017 IEEE International Symposium on Antennas and Propagation & USNC/URSI National Radio Science Meeting*, IEEE, Jul. 2017, pp. 849–850. doi: 10.1109/APUSNCURSINRSM.2017.8072467.
- [10] L. Y. Zhao, L. Y. Xiao, Y. Cheng, R. Hong, and Q. H. Liu, "Machine-Learning-Based Inversion Scheme for Super-Resolution Three-Dimensional Microwave Human Brain Imaging," *IEEE Antennas Wirel Propag Lett*, vol. 21, no. 12, pp. 2437–2441, Dec. 2022, doi: 10.1109/LAWP.2022.3196189.
- [11] M. S. Greeshma and V. R. Bindu, "Super-resolution using Deep Networks for Chest X-Ray Images," in *Proceedings of the IEEE International Conference Image Information Processing*, Institute of Electrical and Electronics Engineers Inc., 2021, pp. 198–201. doi: 10.1109/ICIIP53038.2021.9702582.
- [12] J. Christensen and F. J. García De Abajo, "Slow plasmonic slab waveguide as a superlens for visible light," *Phys Rev B Condens Matter Mater Phys*, vol. 82, no. 16, Oct. 2010, doi: 10.1103/PhysRevB.82.161103.
- [13] R. Dhama, B. Yan, C. Palego, and Z. Wang, "Super-resolution imaging by dielectric superlenses: TiO₂ metamaterial superlens versus batio₃ superlens," *Photonics*, vol. 8, no. 6, Jun. 2021, doi: 10.3390/photronics8060222.
- [14] P. Meng, S. F. Pereira, X. Dou, and H. P. Urbach, "Superresolution effect due to a thin dielectric slab for imaging with radially polarized light," *Opt Express*, vol. 28, no. 14, p. 20660, Jul. 2020, doi: 10.1364/oe.390602.
- [15] N. Waterman, I. Styles, S. Thomas, and S. Zhang, "Super-resolution Imaging with Metamaterials for Cardiovascular Disease," in *Optics in the Life Sciences*, Optica Publishing Group, 2015, p. JT3A.10. [Online]. Available: <https://opg.optica.org/abstract.cfm?URI=NTM-2015-JT3A.10>
- [16] M. G. Silveirinha, C. R. Medeiros, C. A. Fernandes, and J. R. Costa, "Resolving subwavelength objects with a crossed wire mesh superlens operated in backscattering mode," *New J Phys*, vol. 13, May 2011, doi: 10.1088/1367-2630/13/5/053004.
- [17] M. G. Silveirinha, C. A. Fernandes, and J. R. Costa, "Superlens made of a metamaterial with extreme effective parameters," *Phys Rev B Condens Matter Mater Phys*, vol. 78, no. 19, Nov. 2008, doi: 10.1103/PhysRevB.78.195121.
- [18] "CST Microwave Studio™ 2021." [Online]. Available: www.cst.com
- [19] The MathWorks Inc., "MATLAB®2019." [Online]. Available: <https://www.mathworks.com/products/matlab.html>
- [20] J. de S. Marinho, K. Santos, and E. F. da Silva, "Caracterização de Phantoms usando Sonda Coaxial para Aplicações Biomédicas," in *Anais do XXXIX Simpósio Brasileiro de Telecomunicações e Processamento de Sinais*, Sociedade Brasileira de Telecomunicações, 2021, doi: 10.14209/sbrt.2021.1570731660.
- [21] N. Joachimowicz, C. Conessa, T. Henriksson, and B. Duchêne, "Breast phantoms for microwave imaging," *IEEE Antennas Wirel Propag Lett*, vol. 13, pp. 1333–1336, 2014, doi: 10.1109/LAWP.2014.2336373.